Transient Formation of a Second Active Site Cavity during Quinolinic Acid Synthesis by NadA

Hind Basbous, Anne Volbeda, Patricia Amara, Roman Rohac, Lydie Martin, Sandrine Ollagnier de Choudens, Juan-Carlos Fontecilla-Camps

pubs.acs.org/acschemicalbiology

Articles

Transient Formation of a Second Active Site Cavity during Quinolinic Acid Synthesis by NadA

Hind Basbous,[§] Anne Volbeda,[§] Patricia Amara, Roman Rohac, Lydie Martin, Sandrine Ollagnier de Choudens,* and Juan C. Fontecilla-Camps*

Cite This: https://doi.org/10.1021/acschembio.1c00541

Read Online

ACCESS | Metrics & More | Article Recommendations | Supporting Information

ABSTRACT: Quinolinate synthase, also called NadA, is a [4Fe-4S]-containing enzyme that uses what is probably the oldest pathway to generate quinolinic acid (QA), the universal precursor of the biologically essential cofactor nicotinamide adenine dinucleotide (NAD). Its synthesis comprises the condensation of dihydroxyacetone phosphate (DHAP) and iminoaspartate (IA), which involves dephosphorylation, isomerization, cyclization, and two dehydration steps. The convergence of the three homologous domains of NadA defines a narrow active site that contains a catalytically essential [4Fe-4S] cluster. A tunnel, which can be opened or closed depending on the nature (or absence) of the bound ligand, connects this cofactor to the protein surface. One outstanding riddle has been the observation that the so far characterized active site is too small to bind IA and DHAP simultaneously. Here, we have used site-directed mutagenesis, X-ray crystallography, functional analyses, and molecular dynamics simulations to propose a condensation mechanism that involves the transient formation of a second active site cavity to which one of the substrates can migrate before this reaction takes place.

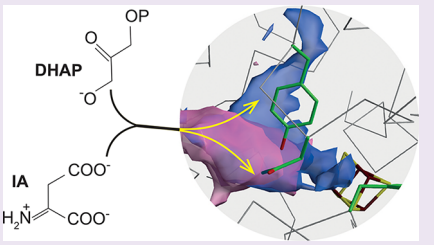

INTRODUCTION

Quinolinic acid (QA) is the precursor of the nicotinamide fragment of the NAD(P) nicotinamide adenine dinucleotide cofactor in all organisms.[1] NAD(P) is involved, through hydride transfer, in many fundamental cellular processes such as respiration and oxidative phosphorylation. The first step of de novo pathway of QA synthesis in prokaryotes is the oxidation of L-Asp by either the flavin-containing enzyme L-Asp oxidase NadB or the NAD-containing L-Asp dehydrogenase NadX to yield iminoaspartate (IA).[2−4] This pathway is found in both bacteria and archaea and is thought to have been the first one to appear during evolution.[5] IA can also be obtained nonenzymatically from the reaction of oxaloacetate with ammonium ions, and this property is sometimes used in in vitro experiments.[6] The next set of reactions in QA synthesis is catalyzed by the enzyme quinolinate synthase, also called NadA, and starts with the condensation of IA with dihydroxyacetone phosphate (DHAP).

NadA coordinates a [4Fe-4S] cluster through three cysteine ligands, leaving one iron ion-binding site available for Lewis-type chemistry.[7,8] As depicted in Figure 1a, this multifunctional enzyme facilitates the attack of the nucleophilic carbanion at the C3 atom of IA to the phosphate-bearing C1 of DHAP(I); this produces the condensed intermediate **W**(II), and as it has been structurally shown by us, it also catalyzes the keto-aldo isomerization of **W**[9,10] to form the **X** intermediate (III). Next, the cluster-bound **X** undergoes dehydration and formation of a Schiff base, followed by (IV) cyclization to generate the **Y** intermediate. Finally, a new dehydration reaction (V) yields the final product, QA.

So far, the structural work has concentrated on quinolinate synthases from two hyperthermophilic microorganisms: the archaeon *Pyrococcus horikoshii* (*Ph*) and the bacterium *Thermotoga maritima* (*Tm*). The first reported NadA structure was the one of apo *Ph*NadA (lacking its [4Fe-4S] cluster) in complex with the serendipitously bound IA analogue L-malate.[11] The first crystal structure of a holo quinolinate synthase, that of the *Tm*NadA K219R variant (hereafter called *Tm*NadA*), was published by us in 2014.[12] NadA is made of three homologous domains, which converge to form an active site cavity that we named cavity I (Figure 1b).[13] The three cluster-coordinating cysteine ligands are located at the C-terminal region of each of these domains, and the unique iron from the [4Fe-4S] cluster is found at the end of a tunnel that connects cavity I with the protein surface.

The comparison of the L-malate-bound apo *Ph*NadA structure with our unliganded holo *Tm*NadA* structure showed that two regions near the active site entrance adopt quite different conformations.[12] As shown in Figure 1c, in the former, the access to this site is blocked mostly by a shift of α-

Received: July 13, 2021
Accepted: September 16, 2021

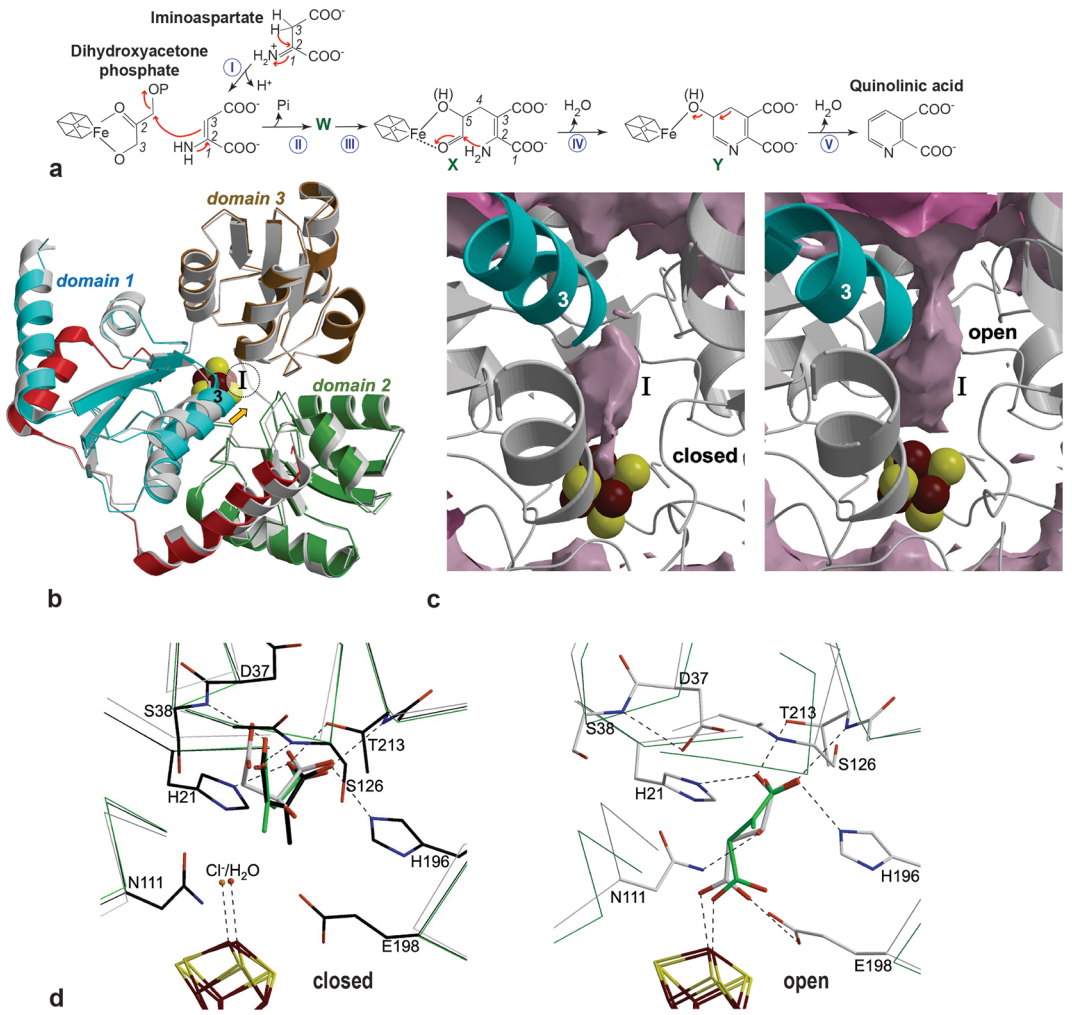

Figure 1. (a) Generally accepted de novo pathway of QA synthesis from IA and dihydroxyacetone phosphate in prokaryotes[16] (see text). (b) NadA domain organization around the active site with superposition of the closed citrate-bound form of *Tm*NadA*Y21F (pdb code 5lqm)[13] to the *Tm*NadA* open form (pdb code 4p3x).[12] The three domains and the C-terminal region of *Tm*NadA*Y21F are sequentially colored cyan, green, and hazel brown; *Tm*NadA* is shown in gray. Secondary structure elements are shown as ribbons for α-helices of at least eight residues and arrows for β-strands longer than two residues; the remaining elements are depicted as lines. The dashed circle highlights active site cavity I, and the orange arrow depicts the movement of helix 3 that closes the connection of this cavity to the protein surface. (c) Cavity change in closed (left, pdb code 5lqm) and open (right, *Tm*NadA*Y107F, see below) tunnel structures. **I** designates active site cavity I, here with the citrate ligand removed (see text). (d) Conformations of IA analogues in left: closed "bent-mode" binding of L-malate (gray carbon atoms, in apo enzyme, pdb code 1wzu),[11] citraconate (black C atoms, pdb code 5kts), and itaconate (green C atoms, pdb code 5ktp);[15] and right: open "straight-mode" binding of L-malate (gray C)[15] and the very similar alternative "straight" binding for itaconate in *Ph*NadA (green).[17] Holo-*Ph*NadA cavity I environments are shown for pdb codes 5kts (citraconate complex, left) and 5ktt (L-malate complex, right).

helix 3 (closed structure, Figure 1b), whereas in the latter, the site is accessible (open structure). Additional closed and open [4Fe-4S]-containing NadA structures have been reported for both quinolinate synthases.[13−15] Those discussed in this work are listed in Table S1.

The IA analogues citraconate and itaconate bind in a "bent" mode closing the NadA structure.[15] This binding is characterized by the interaction of one of the carboxylate groups of the analogue with the main chain N and side chain Oγ1 atoms of *Ph* Thr213 and the imidazole rings of His21 and His196; the other carboxylate interacts with the Ser38 and Ser126 main chain N atoms (Figure 1d, left). In complexes of *Ph*NadA with DHAP,[15] the enzyme is also in the closed conformation with one of the O atoms of the phosphate group interacting with the Oγ1 of Thr213 and the imidazole ring of His21, the second one with the main chain N atom of Ser38 and the third one with the main chain N of Thr213, and the imidazole ring of His196 and the Oγ atom of Ser126 (Figure S1). In addition to adopting the "bent" mode in a closed apo enzyme structure, L-malate can bind to open holo NadA in an approximately "straight" configuration displaying only the first set of carboxylate interactions described above (Figure 1d, right).[15] In this configuration, its second carboxylate group coordinates the [4Fe-4S] cluster. A variant of the open NadA conformation is found with the **X** and **Y** intermediates of QA synthesis.[10] In this case, in addition to the conserved interaction of one of the carboxylate groups of the ligand with the main chain N and side chain Oγ1 of *Tm* Thr211 and the imidazole ring of His19, the second carboxylate interacts with the main chain N and the Oγ atoms of Ser36.

High-resolution structures of *Ph*NadA with bound QA, maleate, and citraconate (pdb codes 5kto, 5ktr, and 5kts)[15] have unveiled the formation of a second active site cavity that we named cavity II.[10] We reasoned that a transient additional

https://doi.org/10.1021/acschembio.1c00541
ACS Chem. Biol. XXXX, XXX, XXX−XXX

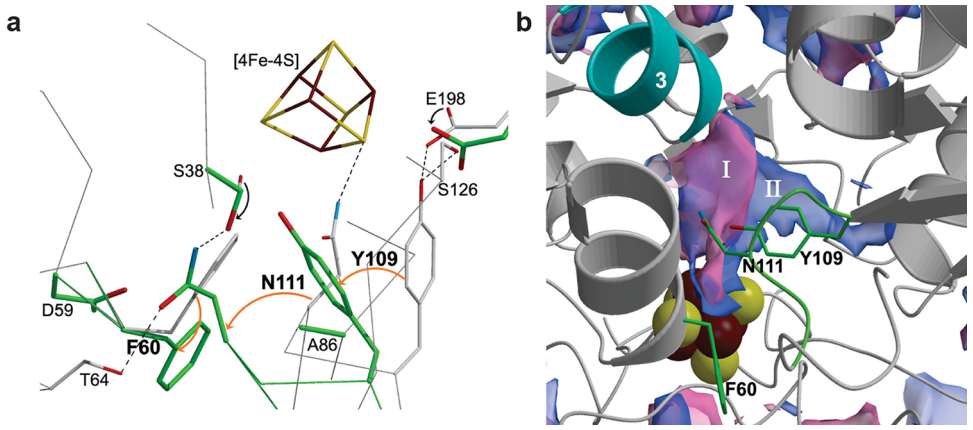

Figure 2. (a) Concerted movement of Tyr109, Asn111, and Phe60 (orange arrows) in a citraconate-*Ph*NadA complex (pdb code 5kts)[15] (gray: commonly observed positions, here called the *a*-structure; green: positions adopted in this structure to form cavity II, called the *b*-structure); see text. (b) Blue surface shows the active site cavity II extension connected to cavity I (pink) of the closed form in the *a*-structure [gray carbons in (a)].

cavity might explain the conundrum that both DHAP and IA analogues have been observed to bind to the *same* pocket in the active site cavity I when cocrystallized with the enzyme or in NadA crystals soaked with these ligands.[15] Indeed, cavity II should add enough space at the active site region to allow for the simultaneous binding of the two substrates prior to their condensation and the concerted phosphate elimination step[10] (Figure 1a). Here, we have used site-directed mutagenesis, X-ray crystallography, structural and functional analyses, and molecular dynamics (MD) simulations to explore the functional relevance of this transient cavity.

RESULTS AND DISCUSSION

Our structural analysis reveals that cavity II is formed by the movement of *Ph*NadA Tyr109, Asn111, and Phe60 (Figure 2a). Here, we have named this local process the "*a*- to *b*-structure transition." The most remarkable conformational change is the 124° rotation of the side chain of Phe60 (Table S2), which facilitates the shift of Asn111 toward the space liberated by the phenylalanine side chain, followed by a concerted Tyr109 displacement. As a result, the region previously occupied by this tyrosine residue, contiguous to cavity I, is now, in principle, available for additional substrate binding (Figure 2b).

Using a new structure of the *Tm*NadA*Y107F variant,[13] we obtained an improved model for the open form of the enzyme (Table 1). A 500 ns MD simulation performed on this open model, where Tyr107 (equiv. to *Ph*Tyr109) was modeled (see the Methods section for details), showed an equivalent Phe58 (equiv. to *Ph*Phe60) rotation without the concomitant movement of Tyr107 and Asn109 (equiv. to *Ph*Asn111) (Figure 3 and Figure S2). This indicates that this rotation, which is essential for cavity II formation, neither depends on nor induces the conformational changes of Tyr107 and Asn109, which generate cavity II.

Mechanism of Cavity II Formation. An exhaustive analysis of published NadA structures shows that three *Ph*NadA liganded structures display cavity II (pdb codes QA: 5kto, citraconate: 5kts and maleate: 5ktr). In the QA-*Ph*NadA complex, the cavity II configuration is fully occupied, whereas in the enzyme with bound citraconate and maleate it has partial occupancy. The QA complex was obtained through cocrystallization, whereas the maleate and citraconate complexes were generated by soaking these IA analogues into previously grown uncomplexed *Ph*NadA crystals.[15] From these observations, it is reasonable to postulate that (i) the crystallizing QA-*Ph*NadA complex formed cavity II in solution

Table 1. X-Ray Data and Refinement Statistics

*Tm*NadA*-variant	Y107F	A84L	S124A
pdb code	7p4m	7p4p	7p4q
data collection			
synchrotron beamline	ESRF ID23-1	ESRF ID23-1	SOLEIL PX2A
wavelength (Å)	0.9760	0.7749	0.9999
detector	Pilatus 6M	Eiger2 16M	Pilatus 6M
space group	$P2_1$	C2	$P2_1$
cell dimensions			
a, *b*, *c* (Å)	55.4, 49.1, 60.8	102.8, 49.2, 69.7	55.7, 49.3, 62.2
α, β, γ (°)	90, 106.8, 90	90, 108.1, 90	90, 108.1, 90
unique reflections	44,673 (4354)	33,318 (3180)	16,403 (1585)
resolution (Å)	49.05−1.55	48.84−1.75	59.15−2.20
high-resolution shell	(1.60−1.55)	(1.81−1.75)	(2.28−2.20)
R_{merge} (%)[aa]	2.8 (49.8)	6.6 (88.8)	8.3 (35.1)
mean $(I/\sigma(I))$[aa]	14.7 (1.6)	10.5 (1.6)	14.2 (3.9)
CC(1/2)[aa]	0.996 (0.608)	0.995 (0.643)	0.995 (0.897)
completeness (%)[aa]	98.1 (97.8)	99.2 (97.3)	99.2 (98.6)
redundancy[aa]	2.6 (2.6)	4.9 (4.9)	5.0 (4.7)
refinement			
resolution (Å)	46.48−1.55	48.84−1.75	59.15−2.20
reflections for R_{work}	42,437	31,660	15,601
R_{work} (%)	13.3	17.1	17.9
reflections for R_{free}	2220	1651	802
R_{free} (%)	17.8	20.3	22.3
no. atoms	2885	2791	2805
average B-factor (Å^2)	37.8	36.7	35.7
r.m.s. deviations			
bond lengths (Å)	0.005	0.006	0.006
bond angles (°)	0.85	0.82	0.78
clashscore	1.36	1.62	2.77
Ramachandran			
favored (%)	99.34	98.02	99.00
outliers (%)	0.00	0.00	0.00
rotamer outliers (%)	0.35	0.37	1.10

[a]Values in parentheses are for the highest-resolution shell.

https://doi.org/10.1021/acschembio.1c00541
ACS Chem. Biol. XXXX, XXX, XXX−XXX

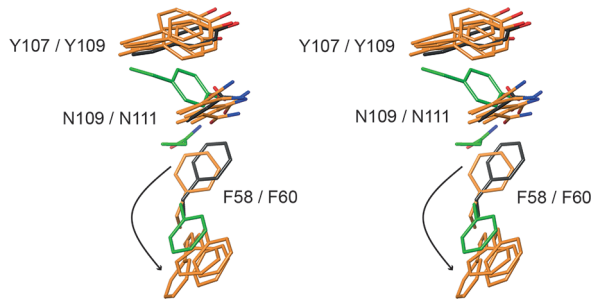

Figure 3. Stereo view of the alternative conformations of Tyr109, Asn111, and Phe60 in the citraconate-*Ph*NadA complex named *a*- and *b*-structures (pdb code 5kts). The two observed conformations of Phe60 are represented in dark gray and green, respectively. Some frames (shown in orange), extracted from the MD trajectory of open *Tm*NadA*, show that while Tyr107 and Asn109 stay roughly in the same conformation, Phe58 can rotate (observed at around 100 and 400 ns, Figure S2), adopting a conformation similar to the one observed in the citraconate-*Ph*NadA complex *b*-structure that displays cavity II (green, closed *b*, pdb code 5kts in Tables S1 and S2).

and (ii) the soaked *Ph*NadA crystals were initially in the open configuration without a bound ligand. The formation of cavity II would have taken place in these crystals upon ligand soaking, and its partial occupancy is consistent with the mixture of open and closed protein states that we have observed in these structures (Figure S3). We do not see cavity II in the crystals of (closed) citrate-*Tm*NadA* and DHAP-*Ph*NadA complexes probably because these molecules interact with residues involved in its formation, forcing the protein to remain in its *a*-structure. Indeed, citrate forms a strong hydrogen bond with the amide Nδ2 from *Tm* Asn109 (Figure S4), and DHAP binds the carboxylate group of *Ph* Glu198 (Figure S1).

The mixed closed/open citraconate-*Ph*NadA complex shows that in its open protein configuration, the passage of *Ph* Asn111 from the *a*- to the *b*-structure (coded gray to green in Figure 2a) is not possible because of a potential clash between its amide Nδ2 and the Cβ/Oγ atoms of Ser38 (Figure S5). This does not happen when the protein structure is closed and implies that cavity II cannot form when NadA is in its open form. When α-helix 3 moves toward cavity I, to adopt the enzyme closed conformation (orange arrow in Figure 1b), the main chain NH of *Ph* Ser38 or *Tm* Ser36 forms a hydrogen bond with one of the O atoms from the carboxylate group of either QA, citrate, citraconate or maleate, or the phosphate group of DHAP.[13,15] The electrostatic attraction toward the carboxylate or phosphate function, resulting from the α-helix δ^+ dipole, could be the driving force for this shift and the ensuing formation of this hydrogen bond, as shown in other systems.[18] Local conformational changes leading to cavity II formation are shown in Figure 2a.

Possible Role of Cavity II in Catalysis. In order to investigate the possible role of cavity II in catalysis, we prepared four groups of *Tm*NadA variants expected to have either an effect on the generation of this cavity or modify its affinity for either DHAP or IA (see Methods): (i) *Tm* D57E and D57M, (ii) *Tm* A84L and A84I, (iii) *Tm* S124A, and (iv) *Tm* F58A (respectively equivalent to *Ph* D59, A86, S126, and F60 in Figure 2a). Glu57 and Met57 would interact with the rotated Phe58, whereas the hydrophobic Leu84 and Ile84, being bulkier than Ala84, should hinder its rotation, thus preventing cavity II formation. Conversely, and based on a previous molecular docking calculation,[10] the absence of the serine Oγ atom in Ala124 could remove an interaction with one of the substrates at cavity II. Finally, F58A is a rather radical variant that could play a local destabilizing role. All the purified variants were reconstituted with adequate [4Fe-4S] cluster concentrations (Figure 4a). The most striking drop of

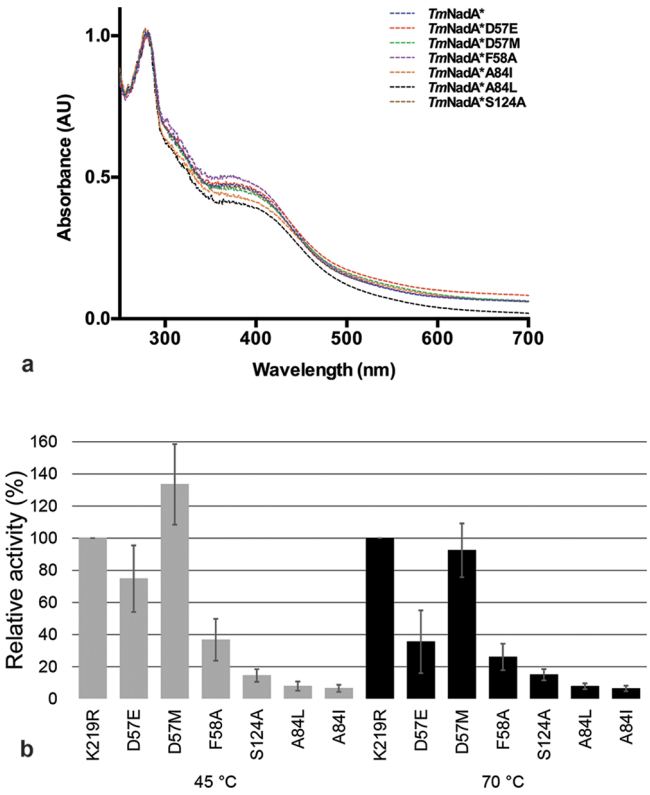

Figure 4. Characterization of *Tm*NadA* and *Tm*NadA* variants. (a) UV−visible spectra after chemical reconstitution. All the proteins (3 mg mL^{-1}) were prepared in buffer B (see the Methods section). (b) Catalytic activity of *Tm*NadA* and its variants at 45 °C (gray bars) and 70 °C (black bars). Specific activity values are reported for the same [4Fe-4S] cluster concentration. The 100% relative activity corresponds to 6.6 and 10.8 nmol min^{-1} mg^{-1} at 45 and 70 °C.

catalytic activity, at both 45 and 70 °C, is observed for the *Tm*NadA*A84L and A84I variants, which display over 90% loss of activity, followed by the S124A variant with 85% activity reduction (Figure 4b). The functional results obtained with these variants support our earlier proposition that cavity II could lodge, at least partially, either IA or DHAP during the condensation reaction[10] (Figure 1a).

The substitutions at *Tm* position 57 have different relative activities, depending on the applied temperature (Figure 4b). The slight drop in activity observed for the D57E variant at 45 °C could be explained by a limited hindrance on Phe58 rotation because of a longer side chain. Conversely, the rather surprising increase in QA synthesis for the D57M variant needs a different explanation. We speculate that a hydrophobic interaction between the side chains of *Tm* Met57 and Phe58, like the one described by Tatko and Waters for a protein beta-hairpin,[19] could stabilize the latter in the cavity II-required rotated position (Figure 2a and Figure S6). This, in turn, would facilitate the formation of that cavity and the ensuing ligand binding and QA synthesis. At the physiologically relevant 70 °C temperature, a higher hindrance by a more agitated Glu57 and a reduced Met57-Phe58 interaction might

https://doi.org/10.1021/acschembio.1c00541
ACS Chem. Biol. XXXX, XXX, XXX−XXX

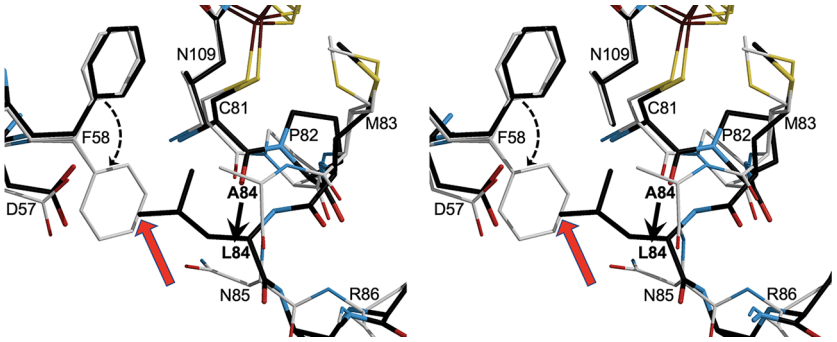

Figure 5. Stereo depiction of the superposition of citrate-bound *Tm*NadA*Y21F (gray-colored carbons, pdb code 5lqm) and the A84L variant (black-colored carbons) structures near Phe58. In the former, Phe58 adopts its two generally observed conformations with similar occupancies (Table S2). The superposition shows that the 124° rotation of Phe58 (from the top left to bottom in the figure, dashed arrow) would cause its collision with Leu84 in the *Tm*NadA*A84L variant (red arrow). The A84L substitution causes a local conformational change (bottom right in the figure), creating a larger pocket that lodges the bulkier Leu side chain. Conversely, the protein regions surrounding the [4Fe-4S] cluster and cavity I remain unchanged (Figure S7a). A different view of this region is shown in Figure S8.

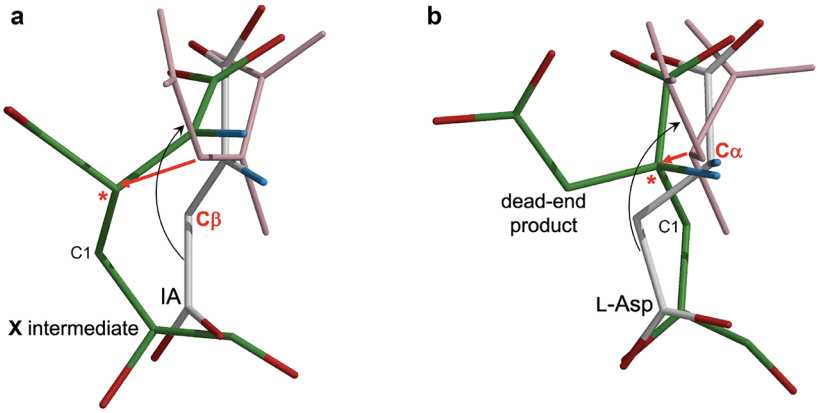

Figure 6. Possible location of IA and L-Asp reactants involved in the generation of (a) the **X** intermediate in *Tm*NadA*[10] and (b) a dead-end product modeled in *Ph*NadA (both depicted with green carbon atoms).[14,17] In a, IA is taken from pdb deposition 6nsu (in the open *Ph*NadA conformation, light gray atoms) and in b, L-Asp is modeled from this proposed IA model (light gray atoms). Rotated positions shown in pink for both IA and L-Asp are modeled from citraconate (closed *Ph*NadA conformation, pdb code 5kts). The carbon atoms that reacted with the labeled C1 carbon atom of DHAP are highlighted with an asterisk (Cβ in IA and Cα in L-Asp).

be expected. The increase in temperature would augment inhibition in the former and diminish the stabilization of the rotated Phe58 in the latter and is consistent with the observed activities (Figure 4b). The activity of the F58A substitution is not surprising because removing the bulky phenylalanine side chain is likely to introduce some local stereochemical instability. However, we have not explored this possibility any further.

Structures of Variant Proteins. In order to further characterize two of the most interesting variants, we determined the crystal structures of the *Tm*NadA*A84L and S124A variants in complex with citrate (added to facilitate their crystallization[13]). The comparison of the former with the corresponding citrate-*Tm*NadA*Y21F complex strongly suggests that the A84L substitution does not affect ligand binding to cavity I. Indeed, we noticed that citrate adopts almost identical conformations in the crystal structures of the two variants (Figure S7a). Conversely, the citrate-*Tm*NadA*A84L structure, which does not display the Phe58 double conformation seen in the citrate-*Tm*NadA*Y21F complex, confirms our prediction that the Leu side chain should block the rotation of this residue (thereby impairing the formation of cavity II, Figure 5). The electron density map indicates that the unique Fe ion of the [4Fe-4S] cluster is fully occupied (Figure S7a).

The structure of the *Tm*NadA*S124A variant in complex with citrate (Figure S7b) is isomorphous with the unliganded open protein structures [pdb code 4p3x and new *Tm*NadA*Y107F variant structure (Table 1)]. In *Tm*NadA*S124A, the unique Fe loss is estimated at about 35%. However, the initial sample had chemically determined 3.1 Fe ions per molecule, a value commonly found in *Tm*NadA preparations with a close to fully occupied [4Fe-4S] cluster (see the Methods section). Consequently, the 85% drop of catalytic activity relative to *Tm*NadA* observed for this variant (Figure 4b) should be mostly due to the removal of the Ser124-OH group. Indeed, the absence of the hydroxyl function reorients the citrate ligand, causing the enzyme to adopt its open configuration (Figure S7b), instead of the closed one observed with other citrate-*Tm*NadA* complexes.[13] In *Tm*NadA*-S124A, citrate binds the enzyme in an orientation similar to the one adopted by **X**[10] (pdb code 6f48) (Figure S7b). Taken together, these results strongly suggest that Ser124 is instrumental in properly orienting at least one of the substrates in the active site before the condensation reaction (step II in Figure 1a). As mentioned above, our previous molecular docking calculation suggested that this residue could be a part

https://doi.org/10.1021/acschembio.1c00541
ACS Chem. Biol. XXXX, XXX, XXX−XXX

Scheme 1. Condensation Reaction Mechanism in QA Synthesis Based on the Functional and Structural Studies Reported in This Study[a]

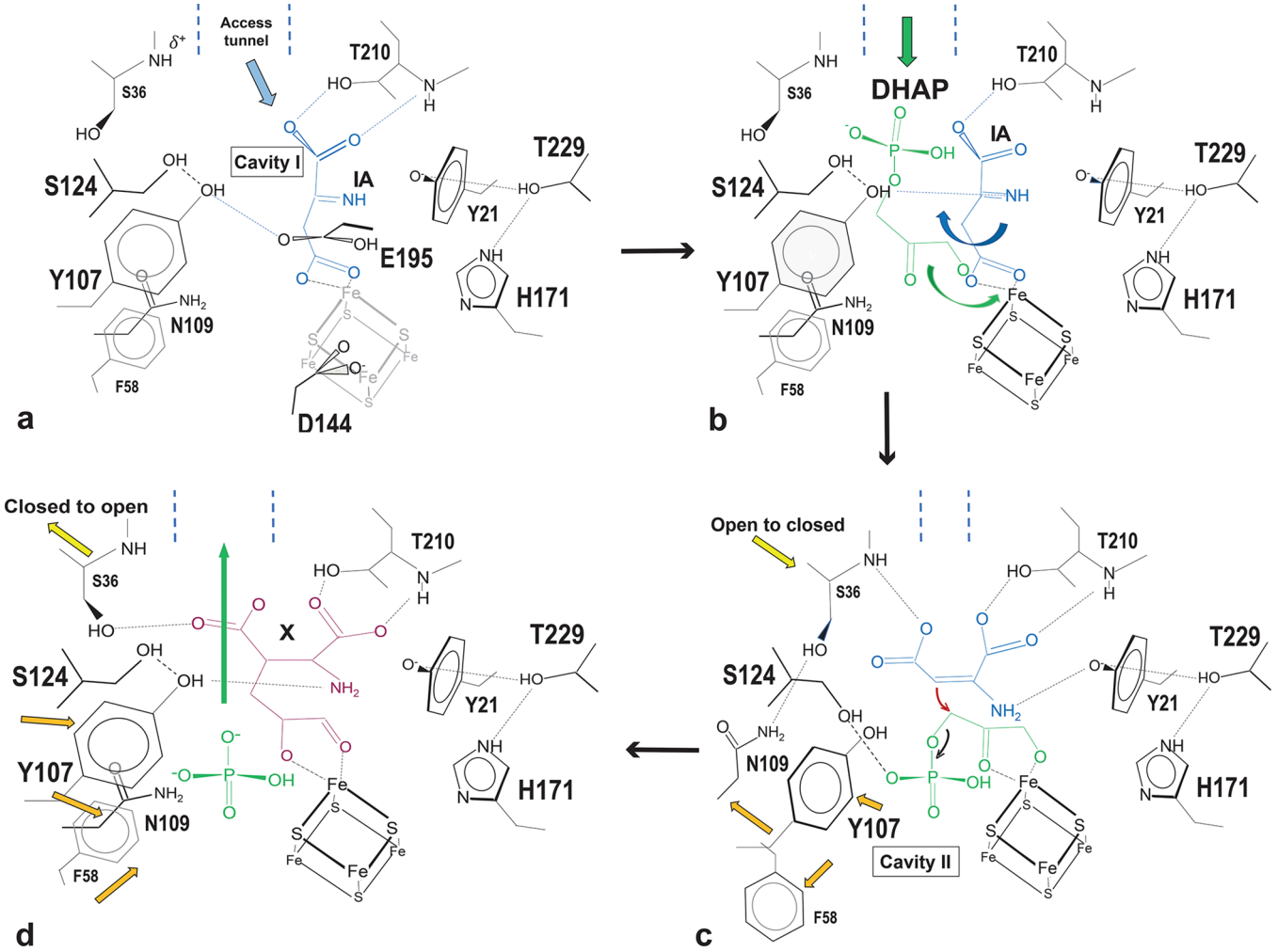

[a](a) IA binds to NadA active site cavity I like L-malate does (Figure 1d, right);[15] (b) DHAP diffuses through the open tunnel and displaces the IA cluster-bound carboxylate; (c) IA adopts a citraconate-like conformation (Figure 1d, left), NadA shifts to its closed conformation, cavity II is formed, DHAP binds both the cluster and cavity II, and condensation takes place; (d) NadA switches back to its open configuration, phosphate is eliminated toward the solvent medium, and the resulting **W** intermediate (not shown) undergoes keto-aldo isomerization, generating the **X** intermediate which is bound at cavity I.

of cavity II.[10] Nevertheless, it is difficult at this point to assign a specific role to Ser124 during catalysis.

Substrate Binding Sequence. We have already proposed that IA binds first to cavity I, adopting a bent conformation similar to citraconate (pdb code 5kts), to be subsequently displaced by DHAP toward cavity II.[10] However, it is also possible that IA initially binds simultaneously to the [4Fe-4S] cluster and the entrance of cavity I, in the open enzyme configuration, adopting a "straight" conformation like L-malate (pdb code 5ktt) does[15,17] (Figure 1d, right). IA would then be displaced from its cluster-binding site by DHAP, perhaps adopting at that point the citraconate-like bent conformation (Figure 1d, left) and subsequently shifting to cavity II. The two substrates would thus be properly poised for condensation to occur.

In our reinterpretation of the reaction that produced a dead-end intermediate in *Ph*NadA[17] (Scheme S1), L-Asp bound in a "straight mode", like L-malate and itaconate shown in Figure 1d (right), would have been displaced by DHAP, adopting a "bent-mode" citraconate-like configuration (Figure 1d, left and Figure 6) during the soaking of the respective crystal in the DHAP-containing cryo-protecting solution.[14] This position of L-Asp would be equivalent to the productive one with IA. However, because of the enolization of the Cα-bound carboxylate group,[17] the reactive nucleophilic species would have been the Cα of L-Asp and not the Cβ, as in IA (compare Figure 1a with Scheme S1). In order for this nonphysiological condensation reaction to occur, the cluster-bound DHAP should have its electrophilic C1 carbon in a position that could be attacked by *both* the enolized Cα of L-Asp and the C3 of IA (Figure 1a, respectively, labeled Asp-Cα and IA-Cβ in Figure 6). This should only be possible if L-Asp and IA are bound to cavity I during the condensation reaction (moving the former to cavity II would not place its Cα in a position compatible with condensation). Thus, cavity II would (partially) bind the phosphate group of DHAP; IA would then stay in cavity I. If this proposition is correct, the previously observed DHAP phosphate-binding mode to *Ph*NadA[15] would be an artifact, resulting from the absence of IA and the similar binding characteristics of the two substrates.

https://doi.org/10.1021/acschembio.1c00541
ACS Chem. Biol. XXXX, XXX, XXX−XXX

CONCLUSIONS

In this work, we have explored the hypothesis that cavity II is essential for catalysis through site-directed mutagenesis, X-ray crystallography, functional analyses, and MD simulations. All the indirect evidence we have been able to gather points at the central role that this cavity plays in providing enough space for the condensation of DHAP and IA within NadA. Because the Phe58 rotation is also observed in the citrate-*Tm*NadA*Y21F complex (pdb code 5lqm), it is clear that this conformational change allows for the formation of cavity II, but it does not elicit it. Furthermore, we have been able to reproduce the rotation of Phe58 with MD simulations on a new high-resolution open structure of the *TmNadA**Y107F variant in which cavity I is only occupied by water and a Cl^- ion (Figure 3). From this observation, we conclude that Phe58 rotation does not depend on the open/closed status of NadA. Conversely, the concerted shift of *Tm* Tyr107 and Asn109 (*Ph* Tyr109 and Asn111) that creates cavity II is only possible in the closed form because of steric hindrance in the open structure between the side chains of *Ph* Ser38 and Asn111 (Figure S5). Enzymes with ligands such as citraconate (pdb code 5kts) and maleate (pdb code 5ktr), that bind at the "top" of cavity I (Figure 1d, left), and QA (pdb code 5kto), which binds to the unique Fe ion from the [4Fe-4S] cluster, displays cavity II.[15] In all these cases, one of the carboxylate groups of the ligand binds the main chain amide N(H) of Ser38. The shift of α-helix 3 toward the active site (Figure 1b), which closes NadA and is required to form that bond, is most probably determined by the expected strong positive potential[18] located at the amide N(H) of *Ph* Ser38 or *Tm* Ser36. In the open L-malate-*Ph*NadA structure, N(H) interacts with the carboxylate group of Asp39 (pdb code 5ktt, Figure 1d, right), which will also compensate for the helical δ^+ effect.

Although both the *Tm* citrate[13] and *Ph* DHAP[15] NadA complexes are in the closed configuration, they do not display cavity II. As mentioned above, we think the reason is that these ligands interact with residues involved in the generation of that cavity, *Tm* Asn109 and *Ph* Glu198, (Figures S4 and Figure 1, respectively). It is tempting to speculate that by preventing cavity II formation when DHAP binds first, NadA imposes the productive binding sequence IA, followed by DHAP.

The revised condensation reaction of the QA synthesis pathway considers both the information gathered from the revised structures obtained using data from refs 14, 15., and the new data presented here are depicted in Scheme 1. In summary, we believe that we have provided convincing indirect evidence that NadA regulates substrate binding through concerted movements that lead to the creation of a transient, and essential, additional active site cavity. This strategy has been seldom observed in enzyme catalysis.[20]

Lastly, an intriguing observation in *Escherichia coli* (*Ec*) NadA is the catalytic activity dependence on the redox status of a Cys-Arg-Ser-Cys sequence in a 10-residue-long loop absent from the *Tm* enzyme.[8] In the *Ec*NadA enzyme, and other ones from related organisms that also have this insertion, the highly conserved Ala84 is replaced by Asp. This observation raises the possibility of a redox-dependent control of cavity II formation in this subclass of quinolinate synthases. We are currently investigating this hypothesis.

METHODS

Strains and Plasmids. *Escherichia coli* BL21(DE3) cells were used to produce the recombinant *Tm*NadA* variants D57E, D57M, F58A, A84I, A84L, and S124A. *E. coli* top10 strains were used to clone the mutants of the *nadA* gene. All products were from Sigma-Aldrich; otherwise, the manufacturer is mentioned.

Cloning of *Thermotoga maritima* NadA Variants. D57E, D57M, F58A, A84I, A84L, and S124A substitutions were introduced in *T. maritima NadA* by PCR using pT7-tmnadAK219R$_{His}$ and the following primers:

D57E: P1 = (5'-CTGTTTCTTGGGGTAGAGTTCATGGCG-GAACTG-3') and P2 = (3'-CCTTCCGTTACCTCGA-GAGTCTTTTCTTTTAA-5').

D57M: P1 = (5'-CTGTTTCTTGGGGTAATGTTCATGGCG-GAACTG-3') and P2 = (3'-CCTTCCGTTACCTCGA-GAGTCTTTTCTTTTAA-5').

F58A: P1 = (5'-CTGTTTCTTGGGGTAGATGCGATGGCG-3') and P2 = (3'-CCTTCCGTTACCTCGAGAGTCTTTTCTTTTAA-5').

A84I: P1 = (5'-CCTGTCCCATGATAAACCGTTTGACACC-3') and P2 = (3'-GCAGGGGCTGTCTTCGCGCCT-5').

A84L: P1 = (5'-CCTGTCCCATGCTGAACCGTTTGACACC-3') and P2 = (3'-GCAGGGGCTGTCTTCGCGCCT-5').

S124A: P1 = (5'-ACGTTATCTGTACGGCTGC-CAACGCCGTGGA-3') and P2 = (3'-GGCTTACGTTTTGC-GAGCGGC-5').

Plasmid sequencing was performed by Eurofins Genomics (Germany), and gene sequences were checked by CLC Sequence Viewer to ensure that no error was introduced during the PCR reaction.

Expression and Purification of *Tm*NadA* and Its Variants. *E. coli* BL21(DE3) competent cells were transformed with pT7-tmnadA$_{His}$ plasmids encoding for *Tm*NadA*, *Tm*NadA*D57E, *Tm*NadA*D57M, *Tm*NadA*F58A, *Tm*NadA*A84I, *Tm*NadA*A84L, and *Tm*NadA*S124A variants. We abbreviate *Tm*NadA K219R to *Tm*NadA* that is functionally equivalent to wild-type enzymes.[12]

Cells were grown aerobically at 37 °C in the LB (Luria Bertani, Miller) medium containing 100 μg mL^{-1} ampicillin to an OD_{600nm} = 0.4; the protein expression was induced with 0.5 mM IPTG (isopropyl 1-thio-β-D-galactopyranoside), and cultures were shaken for 3 h. The induced cells were harvested by centrifugation at 4 °C at 5000 rpm for 20 min, and the pellets were conserved at −80 °C until use. The pellets were suspended aerobically in buffer A (Tris−HCl 100 mM, NaCl 50 mM pH 8) supplemented with 60 mg of lysozyme (Euromedex) and one tablet of complete protease inhibitor cocktail (Roche). Cell disruption was achieved by sonication for 40 cycles on/off of 7 s each at 4 °C, followed by ultracentrifugation at 40,000 rpm at 4 °C for 30 min. The DNA was removed by streptomycin treatment (2%), followed by centrifugation at 8500 rpm at 4 °C for 30 min. The supernatant was heated for 15 min at 75 °C, then cleared by ultracentrifugation at 40,000 rpm at 4 °C for 40 min. The clear supernatant was then loaded on a Ni-nitrilotriacetic acid (NTA) column equilibrated with buffer A. After washing, the proteins were eluted with buffer A containing 300 mM imidazole. Imidazole was removed by passage through an NAP-25 desalting column (GE Healthcare) equilibrated with buffer A. Pure fractions of protein were concentrated and stored at −80 °C until [Fe-S] cluster reconstitution.

Chemical Reconstitution of *Tm*NadA* and Variant Proteins. Reconstitution was performed anaerobically in a glovebox (GB) kept at room temperature (RT) (Jacomex, France). Briefly, 150 μM *Tm*NadA WT (K219R) and variants were incubated with 5 mM DTT (dithiothreitol) (Euromedex) for 30 min in the GB. Then, six equivalents of Mohr's salt and L-cysteine hydrochloric hydrate were added with 1.5 μM *Ec*IscS and incubated for 4 h at RT. Mohr's salt and L-cysteine excess were removed using an NAP-25 desalting column equilibrated with buffer B (Tris−HCl 20 mM, NaCl 150 mM, pH 8). Then, the protein was heated at 65 °C for 20 min in the presence of 50 mM DTT and centrifuged at 10,000 rpm for 15 min in the GB. The dark sample was then loaded on a Superdex75 (GE Healthcare) column with buffer C (Tris−HCl 125 mM, KCl 50 mM, pH 8). Holo-monomeric NadA fractions were pooled, concentrated to 20 mg mL^{-1}, aliquoted, and stored at −80 °C.

https://doi.org/10.1021/acschembio.1c00541
ACS Chem. Biol. XXXX, XXX, XXX−XXX

[4Fe-4S] cluster integrity was checked by ultraviolet−visible (UV−vis) absorption spectroscopy and iron content. The chemically determined iron content per monomer of these reconstituted proteins is as follows: *Tm*NadA* (3.3 Fe), *Tm*NadA*D57E (3.2 Fe), *Tm*NadA*D57M (3.2 Fe), *Tm*NadA*F58A (3.3 Fe), *Tm*NadA*A84I (4.3 Fe), *Tm*NadA*A84L (3.1 Fe), and *Tm*NadA*S124A (3.1 Fe).

Protein Analysis. Protein concentrations were measured using the method of Bradford using bovine serum albumin as a standard and applying correction factors for NadA, as previously described.[21] Protein-bound iron was determined under reducing conditions with bathophenanthroline disulfonate after acid denaturation of the protein.[22] UV−visible spectra were recorded with a Cary 1 Bio (Varian) spectrophotometer.

In Vitro Quinolinate Synthase Activity of *Tm*NadA* Proteins. Enzymatic characterization of the quinolinate synthase activity of *Tm*NadA* and variants was performed anaerobically in the GB using the chemical condition for IA synthesis. NadA (20 μM) was mixed in a final volume of 100 μL of buffer D (50 mM Na-HEPES, 100 mM KCl pH 7.5) with 2 mM DHAP, 5 mM oxaloacetic acid (OAA), and an excess (10 mM) of ammonium sulfate (AS) to chemically generate IA. The mixture was incubated for 20 min at 45 or 70 °C, and the reaction was quenched by adding 5 μL of 2 M sulfuric acid and 5 μL of 5 M perchloric acid. After centrifugation (14,000 rpm, 4 °C, 15 min), 50 μL of the supernatant was mixed with 50 μL of buffer E (0.03% trifluoroacetic acid, pH 2.4) and injected on a Supelcogel column equilibrated with buffer E. QA elution was eluted at a flow rate of 0.17 mL min^{-1} using buffer E and quantified using a standard curve of 0 to 20 nmol of commercial QA, allowing for the determination of NadA-specific activity (nmol mg^{-1} min^{-1}).

Biochemical and Functional Analyses of *Tm*NadA* Variants. Single substitutions introduced in *Tm*NadA* did not affect the expression of proteins nor their solubility, and in all cases, very good purification yields were obtained (Table S3). In addition, all *Tm*NadA* variants were obtained with good purity, as shown by sodium dodecyl sulfate−polyacrylamide gel (SDS-PAGE) electrophoresis (Figure S9). Purified *Tm*NadA* variants are in the apo-form as is *Tm*NadA* (our control). [Fe-S] cluster reconstitution was performed in the GB in the presence of six equivalents of ferrous iron salt and sulfide, catalytically generated by IscS from L-cysteine. After gel-filtration, each *Tm*NadA* variant monomer had a yellow-brownish color and exhibited some of the biochemical and spectroscopic properties of the *Tm*NadA* protein. Indeed, each *Tm*NadA* variant displays a UV−vis spectrum with a unique intense band at 420 nm characteristic of a $[4Fe\text{-}4S]^{2+}$ cluster-containing protein, with a 420/280 nm ratio equal to 0.4−0.5 (Figure 4a). The presence of an intact $[4Fe\text{-}4S]^{2+}$ cluster was confirmed by measuring the iron content of the variants, which was between 3.2 and 4.3 Fe/monomer (Table S3). These analyses demonstrate that the introduced single substitutions have no effect on the degree of $[4Fe\text{-}4S]^{2+}$ prosthetic group incorporation in the *Tm*NadA* variants.

In vitro enzymatic activity of *Tm*NadA* variants was determined using *Tm*NadA* as a positive control. Because *Tm*NadA comes from a hyperthermophilic organism, the activity measurements were performed at 45 and 70 °C in the presence of DHAP and chemically generated IA, respectively. The results show the crucial role Ala84 and Ser124 play in QA formation. Indeed, the residual NadA-specific activity at 45 °C was 8% for the A84L and A84I variants and 15% for the S124A variant (Figure 4b). Similar activities were obtained at 70 °C. The introduction of an alanine residue at the Phe58 position causes a decrease of 63 and 74% of the enzymatic activity at 45 and 70 °C, respectively. The D57E and D57M substitutions have less impact on this activity (Figure 4b).

Cavity Calculations. Cavities were calculated with the homemade program CAVENV, which is a part of the CCP4 package.[23] The cavity maps shown in Figures 1c and 2b were contoured with an accessible probe radius of 1 Å.

Crystallization of the *Tm*NadA*S124A, A84L, and Y107F Variants. Crystallization assays were performed under anaerobic conditions in a GB using the hanging drop vapor diffusion method. For each variant, hanging drops were prepared by mixing 1 μL of the protein solution with an equal amount of the crystallization solution before anaerobic equilibration with 1 mL of the latter. *Tm*NadA*-S124A crystals were obtained from a 20 mg mL^{-1} protein solution in buffer C, pH 8.0, and 100 mM trisodium citrate crystallization solution, pH 5.6, 50 mM NaCl, 100 mM ammonium acetate, and 28 or 30% PEG4000. A 25 mg mL^{-1} protein solution in buffer C was used for the *Tm*NadA*A84L variant, with 1.4 M trisodium citrate, pH 6.0 crystallization solution in buffer C. For the *Tm*NadA*Y107F variant,[13] 100 μL of a 20 mg mL^{-1} protein solution in buffer C, pH 7.2, was incubated anaerobically overnight at 20 °C with 1 μL of 0.5 M AS, 2 μL of 0.5 M oxaloacetate, and 4 μL of 50 mM DHAP. The crystallization solution used for this variant contained 100 mM bis tris propane, pH 6.5, 100 mM (w/v) 29% PEG3350, and 100 mM NaF. The A84L variant crystal was mounted directly from the hanging drop; the other crystals were mounted in loops from a cryo-protecting solution obtained from the crystallization solution supplemented with 25% glycerol for the S124A variant and an additional 11% of PEG3350 for the Y107F variant. Next, the crystals were flash-frozen inside the GB with liquid propane.[24]

X-Ray Structure Determination of the *Tm*NadA*S124A, A84L, and Y107F Variants. X-ray diffraction data (Table 1) were measured at the SOLEIL synchrotron (Saint Aubain, France) and at the ESRF (European Synchrotron Radiation Facility, Grenoble, France) running under MXCuBe,[25] from crystals exposed to a 100 K cold nitrogen stream. All data were indexed, integrated, and scaled with *XDS*[26] and checked for anisotropic diffraction with *AIMLESS*.[27] Crystal structures were solved by molecular replacement using *PHASER*,[28] starting from high-resolution open (pdb 6f48)[10] and closed (pdb 5f33)[13] *Tm*NadA* models. The obtained solutions were next subjected to rigid body refinement with *REFMAC5*[29] and positional and B-factor refinement with *PHENIX* (Adams 2010).[30] In addition to atomic isotropic B-factors, Translation/Libration/Screw (TLS) parameters were refined for the citrate-bound S124A and A84L variants. For the Y107F variant, the resolution was high enough to facilitate the refinement of individual atomic anisotropic B-factors. Manual model corrections were performed with *COOT*.[31] Refinement statistics are included in Table 1. The refined models of the S124A and Y107F variants correspond to open *Tm*NadA* structures, whereas the A84L variant, in complex with citrate, crystallized in a closed form. The crystal structures of the citrate-*Tm*NadA*S124A complex and Y107F *Tm*NadA* revealed losses of the unique Fe of the [4Fe-4S] of about 35 and 45%, whereas its occupancy in the *Tm*NadA*A84L variant was 100%. The crystal of the *Tm*NadA*Y107F variant has a Cl^- ion bound to the cluster unique Fe. Because of its high resolution, we used this structure as a starting model for MD of the open *Tm*NadA form (see the MD Simulations section below). Except for MXCUBE, the software referred to above was compiled by SBGRID (Morin 2013).[32]

Accession Codes. The atomic coordinates and structure factors have been deposited to the PDB (ID codes 7p4m, 7p4p, and 7p4q for the Y107, A84L, and S124A *Tm*NadA* variants, respectively).

Preparation of Figures. Figures 1b,d, 2a, 5, and 6 and Figures S1, S4−S6, and S8 were prepared with MOLSCRIPT,[33] Figures 1c and 2b, and Figure S7 with BOBSCRIPT.[34] All these figures were rendered by *RASTER3D*.[35] Figure S3a,b were prepared with COOT.[31] Figure 3 and Figure S10 were prepared with Maestro.[36]

MD Simulations. Calculations were performed with programs from the Schrödinger suite.[36] Because we wanted to investigate the rotation of Phe58 in an open form of *Tm*NadA, where the formation of cavity II is not possible (see main text), the new *Tm*NadA*Y107F crystal structure was used. It is at a higher resolution than the open *Tm*NadA* (pdb code 4p3x).[12] Their superposition shows that they are very similar, with the exception of a hydrogen bond between the -OH group of Tyr107 and the carboxylate group of Glu195 because of the substitution. Phe107 was *in silico*-substituted by Tyr by adding the phenol −OH group; hydrogen atoms were constructed, and the protonation state of each residue was optimized using the protein preparation protocol. Negatively charged and protonated states were specifically tested for Glu195 because it interacts with the -OH group of Tyr107 and is also close to the conserved Asp144, which was

https://doi.org/10.1021/acschembio.1c00541
ACS Chem. Biol. XXXX, XXX, XXX−XXX

modeled in its deprotonated state. In the Schrödinger suite, by default and for any force field, the charges of [Fe-S] clusters are formal, that is, +2 or +3 for the Fe atoms and −2 for the inorganic bridging S atoms. We know from previous MD studies on the RsrR [FeS]-containing metalloprotein[37] that these formal charges can induce artifactual interactions. Accordingly, we calculated more realistic charges using a small quantum model (Figure S10).

We used a broken symmetry to model the oxidized [4Fe-4S] cluster with the Jaguar QM program.[38] In [4Fe-4S] clusters, the iron ions exhibit local high spin configurations $S = 5/2$ (ferric ion) and $S = 2$ (ferrous ion). The oxidized state consists of two mixed-valence iron pairs, (Fe^{II}-Fe^{III}) of spin $S = 9/2$ each, antiferromagnetically coupled, yielding a cluster with $M_s = 0$.[39] A customized functional with 5% Hartree-Fock exchange combined with the LACVP** basis set was employed to geometry-optimize this model, fixing the Cα and Cβ atoms of the cluster cysteine ligands. Subsequently, the charges were calculated to fit the external electrostatic potential (the so-called ESP charges). We used these charges for our MD simulations.

The OPLS3e force field[40,41] was employed. Na^+ or Cl^- ions were added to neutralize our models that were further solvated with a periodically replicated orthorhombic water box using the Simple Point Charge (SPC) water model. Additional Na^+ and Cl^- ions were added to reach a theoretical salt concentration of 150 mM. The resulting systems consisted of approximately 42,000 atoms.

The Desmond program[42,43] included in the Schrödinger suite was used for MD simulations. The default protocol was used to equilibrate the system and heat it from 0 to 300 K. The simulations were then run for 500 ns with a time step of 2 fs in the isobaric, isothermal (NPT) ensemble with a temperature of 300 K and a pressure of 1 atm. In the MD trajectory at 300 K with a protonated Glu195, the hydrogen bond between the −OH group of Tyr107 and Glu195 sidechains is not maintained. In contrast, the short hydrogen bond between both residues, observed in the first *Tm*NadA* open form (4P3X), remains throughout the MD simulation at 300 K when Glu195 is deprotonated. The analysis of Phe58 dynamics during the MD with Glu195 deprotonated at 300 K shows no rotation of the Phe58 sidechain. In contrast, the same MD simulation, performed at 350 K, closer to the optimal *T. maritima* growth temperature, reveals that Phe58 in a starting conformation, resembling the one in the citraconate-PhNadA complex partial *a*-structure, can rotate and adopt a conformation similar to the one it has in the complex partial *b*-structure (see main text, Figure 3 and Figure S2).

■ ASSOCIATED CONTENT

Supporting Information

The Supporting Information is available free of charge at https://pubs.acs.org/doi/10.1021/acschembio.1c00541.

Additional structural and functional analyses and MD Figures and Tables (PDF).

■ AUTHOR INFORMATION

Corresponding Authors

Sandrine Ollagnier de Choudens − *Univ. Grenoble Alpes, CNRS, CEA, Laboratoire de Chimie et Biologie des Métaux, BioCat, 38000 Grenoble, France*;
Email: sandrine.ollagnier@cea.fr

Juan C. Fontecilla-Camps − *Univ. Grenoble Alpes, CEA, CNRS, IBS, Metalloproteins, F-38000 Grenoble, France*; orcid.org/0000-0002-3901-1378;
Email: juan.fontecilla@ibs.fr

Authors

Hind Basbous − *Univ. Grenoble Alpes, CNRS, CEA, Laboratoire de Chimie et Biologie des Métaux, BioCat, 38000 Grenoble, France*

Anne Volbeda − *Univ. Grenoble Alpes, CEA, CNRS, IBS, Metalloproteins, F-38000 Grenoble, France*; orcid.org/0000-0002-6038-0979

Patricia Amara − *Univ. Grenoble Alpes, CEA, CNRS, IBS, Metalloproteins, F-38000 Grenoble, France*; orcid.org/0000-0001-9634-7305

Roman Rohac − *Univ. Grenoble Alpes, CEA, CNRS, IBS, Metalloproteins, F-38000 Grenoble, France*

Lydie Martin − *Univ. Grenoble Alpes, CEA, CNRS, IBS, Metalloproteins, F-38000 Grenoble, France*

Complete contact information is available at: https://pubs.acs.org/10.1021/acschembio.1c00541

Author Contributions

[§]H.B. and A.V. contributed equally to this work.

Notes

The authors declare no competing financial interest.

■ ACKNOWLEDGMENTS

We thank the CEA and the CNRS for institutional support. The help of M. Pelosse to produce the different *Tm*NadA*variants is greatly appreciated. We also thank the French National Research Agency for contract ANR-16-CE18-0026 (NADIN). S.O.d.C. also acknowledges partial financial support from the ARCANE Labex (ANR-11-LABX-0003-01) and GRAL Labex (ANR-10-LABEX-04 GRAL. Labex, Grenoble Alliance for Integrated Structural Cell Biology). Part of this work used the platforms of the Grenoble Instruct-ERIC center (ISBG; UMS 3518 CNRS-CEA-UGA-EMBL) within the Grenoble Partnership for Structural Biology (PSB), supported by FRISBI (ANR-10-INBS-05-02) and GRAL, financed within the University Grenoble Alpes graduate school (Ecoles Universitaires de Recherche) CBH-EUR-GS (ANR-17-EURE-0003). We appreciate the help from the staff of the ESRF beamlines (Grenoble) with X-ray data collection and of the computing facility provided by the Commissariat à l'Energie Atomique (CEA/DSV/GIPSI), Saclay, and (CCRT), Bruyères-le-Châtel.

■ REFERENCES

(1) Foster, J. W.; Moat, A. G. Nicotinamide adenine dinucleotide biosynthesis and pyridine nucleotide cycle metabolism in microbial systems. *Microbiol. Rev.* **1980**, *44*, 83−105.

(2) Begley, T. P.; Kinsland, C.; Mehl, R. A.; Osterman, A.; Dorrestein, P. The biosynthesis of nicotinamide adenine dinucleotides in bacteria. *Vitam. Horm.* **2001**, *61*, 103−119.

(3) Nasu, S.; Wicks, F. D.; Sakakibara, S.; Gholson, R. K. Synthesis of quinolinate from D-aspartate in the mammalian liver-*Escherichia coli* quinolinate synthetase system. *Biochem. Biophys. Res. Commun.* **1978**, *84*, 928−935.

(4) Yang, Z.; Savchenko, A.; Yakunin, A.; Zhang, R.; Edwards, A.; Arrowsmith, C.; Tong, L. Aspartate dehydrogenase, a novel enzyme identified from structural and functional studies of TM1643. *J. Biol. Chem.* **2003**, *278*, 8804−8808.

(5) Lima, W. C.; Varani, A. M.; Menck, C. F. M. NAD Biosynthesis evolution in bacteria: lateral gene transfer of Kynurenine pathway in Xanthomonadales and Flavobacteriales. *Mol. Biol. Evol.* **2009**, *26*, 399−406.

(6) Nasu, S.; Gholson, R. K. Replacement of the B protein requirement of the E. coli quinolinate synthetase system by chemically-generated iminoaspartate. *Biochem. Biophys. Res. Commun.* **1981**, *101*, 533−539.

(7) Cicchillo, R. M.; Tu, L.; Stromberg, J. A.; Hoffart, L. M.; Krebs, C.; Booker, S. J. *Escherichia coli* quinolinate synthetase does indeed harbor a [4Fe-4S] cluster. *J. Am. Chem. Soc.* **2005**, *127*, 7310−7311.

https://doi.org/10.1021/acschembio.1c00541
ACS Chem. Biol. XXXX, XXX, XXX−XXX

(8) Rousset, C.; Fontecave, M.; Ollagnier de Choudens, S. The [4Fe-4S] cluster of quinolinate synthase from *Escherichia coli*: investigation of cluster ligands. *FEBS Lett.* **2008**, *582*, 2937−2944.
(9) Reichmann, D.; Couté, Y.; Ollagnier de Choudens, S. Dual activity of quinolinate synthase: triose phosphate isomerase and dehydration activities play together to form quinolinate. *Biochemistry* **2015**, *54*, 6443−6446.
(10) Volbeda, A.; Saez Cabodevilla, J.; Darnault, C.; Gigarel, O.; Han, T.-H.-L.; Renoux, O.; Hamelin, O.; Ollagnier-de-Choudens, S.; Amara, P.; Fontecilla-Camps, J. C. Crystallographic trapping of reaction intermediates in quinolinic acid synthesis by NadA. *ACS Chem. Biol.* **2018**, *13*, 1209−1217.
(11) Sakuraba, H.; Tsuge, H.; Yoneda, K.; Katunuma, N.; Ohshima, T. Crystal structure of the NAD biosynthetic enzyme quinolinate synthase. *J. Biol. Chem.* **2005**, *280*, 26645−26648.
(12) Cherrier, M. V.; Chan, A.; Darnault, C.; Reichmann, D.; Amara, P.; Ollagnier de Choudens, S.; Fontecilla-Camps, J. C. The crystal structure of Fe_4S_4 quinolinate synthase unravels an enzymatic dehydration mechanism that uses tyrosine and a hydrolase-type triad. *J. Am. Chem. Soc.* **2014**, *136*, 5253−5256.
(13) Volbeda, A.; Darnault, C.; Renoux, O.; Reichmann, D.; Amara, P.; Ollagnier de Choudens, S.; Fontecilla-Camps, J. C. Crystal structures of quinolinate synthase in complex with a substrate analogue, the condensation intermediate, and substrate-derived product. *J. Am. Chem. Soc.* **2016**, *138*, 11802−11809.
(14) Esakova, O. A.; Silakov, A.; Grove, T. L.; Warui, D. M.; Yennawar, N. H.; Booker, S. J. An unexpected species determined by X-ray crystallography that may represent an intermediate in the reaction catalyzed by quinolinate synthase. *J. Am. Chem. Soc.* **2019**, *141*, 14142−14151.
(15) Fenwick, M. K.; Ealick, S. E. Crystal structures of the iron-sulfur cluster-Dependent quinolinate synthase in complex with dihydroxyacetone phosphate, iminoaspartate analogues, and quinolinate. *Biochemistry* **2016**, *55*, 4135−4139.
(16) Nasu, S.; Wicks, F. D.; Gholson, R. K. L-Aspartate oxidase, a newly discovered enzyme of *Escherichia coli*, is the B protein of quinolinate synthetase. *J. Biol. Chem.* **1982**, *257*, 626−632.
(17) Volbeda, A.; Fontecilla-Camps, J. C. Structural basis for the catalytic activities of the multifunctional enzyme quinolinate synthase. *Coord. Chem. Rev.* **2020**, *417*, No. 213370.
(18) Gunner, M. R.; Saleh, M. A.; Cross, E.; ud-Doula, A.; Wise, M. Backbone dipoles generate positive potentials in all proteins: origins and implications of the effect. *Biophys. J.* **2000**, *78*, 1126−1144.
(19) Tatko, C. D.; Waters, M. L. Investigation of the nature of the methionine−π interaction in β-hairpin peptide model systems. *Protein Sci.* **2004**, *13*, 2515−2522.
(20) Stank, A.; Kokh, D. B.; Fuller, J. C.; Wade, R. C. Protein Binding Pocket Dynamics. *Acc. Chem. Res.* **2016**, *49*, 809−815.
(21) Bradford, M. M. A rapid and sensitive method for the quantitation of microgram quantities of protein utilizing the principle of protein-dye binding. *Anal. Biochem.* **1976**, *72*, 248−254.
(22) Fish, W. W. Rapid colorimetric micromethod for the quantitation of complexed iron in biological samples. *Methods Enzymol.* **1988**, *158*, 357−364.
(23) Winn, M. D.; Ballard, C. C.; Cowtan, K. D.; Dodson, E. J.; Emsley, P.; Evans, P. R.; Keegan, R. M.; Krissinel, E. B.; Leslie, A. G. W.; McCoy, A.; McNicholas, S. J.; Murshudov, G. N.; Pannu, N. S.; Potterton, E. A.; Powell, H. R.; Read, R. J.; Vagin, A.; Wilson, K. S. Overview of the CCP4 suite and current developments. *Acta Crystallogr. D Biol. Crystallogr.* **2011**, *67*, 235−242.
(24) Vernède, X.; Fontecilla-Camps, J. C. A method to stabilize reduced and or gas-treated protein crystals by flash-cooling under a controlled atmosphere. *J. Appl. Crystallogr.* **1999**, *32*, 505−509.
(25) Gabadinho, J.; Beteva, A.; Guijarro, M.; Rey-Bakaikoa, V.; Spruce, D.; Bowler, M. W.; Brockhauser, S.; Flot, D.; Gordon, E. J.; Hall, D. R.; Lavault, B.; McCarthy, A. A.; McCarthy, J.; Mitchell, E.; Monaco, S.; Mueller-Dieckmann, C.; Nurizzo, D.; Ravelli, R. B. G.; Thibault, X.; Walsh, M. A.; Leonard, G. A.; McSweeney, S. M. MxCuBE: a synchrotron beamline control environment customized for macromolecular crystallography experiments. *J. Synchrotron Radiat.* **2010**, *17*, 700−707.
(26) Kabsch, W. XDS. *Acta Crystallogr. D Biol. Crystallogr.* **2010**, *66*, 125−132.
(27) Evans, P. R.; Murshudov, G. N. How good are my data and what is the resolution? *Acta Crystallogr. D Biol. Crystallogr.* **2013**, *69*, 1204−1214.
(28) McCoy, A. J.; Grosse-Kunstleve, R. W.; Adams, P. D.; Winn, M. D.; Storoni, L. C.; Read, R. J. Phaser crystallographic software. *J. Appl. Crystallogr.* **2007**, *40*, 658−674.
(29) Murshudov, G. N.; Skubák, P.; Lebedev, A. A.; Pannu, N. S.; Steiner, R. A.; Nicholls, R. A.; Winn, M. D.; Long, F.; Vagin, A. A. REFMAC5 for the refinement of macromolecular crystal structures. *Acta Crystallogr. D Biol. Crystallogr.* **2011**, *67*, 355−367.
(30) Adams, P. D.; Afonine, P. V.; Bunkóczi, G.; Chen, V. B.; Davis, I. W.; Echols, N.; Headd, J. J.; Hung, L.-W.; Kapral, G. J.; Grosse-Kunstleve, R. W.; McCoy, A. J.; Moriarty, N. W.; Oeffner, R.; Read, R. J.; Richardson, D. C.; Richardson, J. S.; Terwilliger, T. C.; Zwart, P. H. PHENIX: a comprehensive Python-based system for macromolecular structure solution. *Acta Crystallogr. D Biol. Crystallogr.* **2010**, *66*, 213−221.
(31) Emsley, P.; Lohkamp, B.; Scott, W. G.; Cowtan, K. Features and development of Coot. *Acta Crystallogr. D Biol. Crystallogr.* **2010**, *66*, 486−501.
(32) Morin, A.; Eisenbraun, B.; Key, J.; Sanschagrin, P. C.; Timony, M. A.; Ottaviano, M.; Sliz, P. Collaboration gets the most out of software. *Elife* **2013**, *2*, No. e01456.
(33) Kraulis, P. J. MOLSCRIPT: a program to produce both detailed and schematic plots of protein structures. *J. Appl. Crystallogr.* **1991**, *24*, 946−950.
(34) Esnouf, R. M. Further additions to MolScript version 1.4, including reading and contouring of electron-density maps. *Acta Crystallogr. D Biol. Crystallogr.* **1999**, *55*, 938−940.
(35) Merritt, E. A.; Murphy, M. E. Raster3D Version 2.0. A program for photorealistic molecular graphics. *Acta Crystallogr. D Biol. Crystallogr.* **1994**, *50*, 869−873.
(36) *Schrödinger Release 2019−2*. Schrödinger, LLC: New York, NY, 2019.
(37) Crack, J. C.; Amara, P.; Volbeda, A.; Mouesca, J.-M.; Rohac, R.; Pellicer Martinez, M. T.; Huang, C.-Y.; Gigarel, O.; Rinaldi, C.; Le Brun, N. E.; Fontecilla-Camps, J. C. Electron and proton transfers modulate DNA binding by the transcription regulator RsrR. *J. Am. Chem. Soc.* **2020**, *142*, 5104−5116.
(38) Bochevarov, A. D.; Harder, E.; Hughes, T. F.; Greenwood, J. R.; Braden, D. A.; Philipp, D. M.; Rinaldo, D.; Halls, M. D.; Zhang, J.; Friesner, R. A. Jaguar: A high-performance quantum chemistry software program with strengths in life and materials sciences. *Int. J. Quantum Chem.* **2013**, *113*, 2110−2142.
(39) Mouesca, J. M. Density functional theory-broken symmetry (DFT-BS) methodology applied to electronic and magnetic properties of bioinorganic prosthetic groups. *Methods Mol. Biol.* **2014**, *1122*, 269−296.
(40) Harder, E.; Damm, W.; Maple, J.; Wu, C.; Reboul, M.; Xiang, J. Y.; Wang, L.; Lupyan, D.; Dahlgren, M. K.; Knight, J. L.; Kaus, J. W.; Cerutti, D. S.; Krilov, G.; Jorgensen, W. L.; Abel, R.; Friesner, R. A. OPLS3: A force field providing broad coverage of drug-like small molecules and proteins. *J. Chem. Theory Comput.* **2016**, *12*, 281−296.
(41) Roos, K.; Wu, C.; Damm, W.; Reboul, M.; Stevenson, J. M.; Lu, C.; Dahlgren, M. K.; Mondal, S.; Chen, W.; Wang, L.; Abel, R.; Friesner, R. A.; Harder, E. D. OPLS3e: Extending force field coverage for drug-like small molecules. *J. Chem. Theory Comput.* **2019**, *15*, 1863−1874.
(42) Bowers, K. J.; Chow, D. E.; Xu, H.; Dror, R. O.; Eastwood, M. P.; Gregersen, B. A.; Klepeis, J. L.; Kolossvary, I.; Moraes, M. A.; Sacerdoti, F. D.; Salmon, J. K.; Shan, Y.; Shaw, D. E. Scalable Algorithms for Molecular Dynamics Simulations on Commodity Clusters. In *ACM/IEEE SC 2006 Conference (SC'06)*; IEEE: Tampa, FL, 2006; pp. 43−43.

https://doi.org/10.1021/acschembio.1c00541
ACS Chem. Biol. XXXX, XXX, XXX−XXX

(43) Desmond Molecular Dynamics System, D. E. Shaw Research, New York, NY, 2019. *Maestro-Desmond Interoperability Tools*. Schrödinger: New York, NY, 2019.

https://doi.org/10.1021/acschembio.1c00541
ACS Chem. Biol. XXXX, XXX, XXX−XXX